The water-carbon dioxide miscibility surface to 450°C and 7 GPa

E. H. Abramson (corresponding author, e-mail:evan@ess.washington.edu),
O. Bollengier (e-mail: obollengier@gmail.com)
and J. M. Brown (e-mail: brown@ess.washington.edu)

Department of Earth and Space Sciences, University of Washington
Seattle, WA 98195-1310 USA

ABSTRACT
Fluid-fluid immiscibility in the water-carbon dioxide binary system has been measured to a pressure of 7 GPa and temperature of 450°C, providing the first such data under conditions pertinent to subduction zones and the icy worlds of the outer solar system. Water and carbon dioxide were loaded as inhomogeneous mixtures in externally-heated diamond-anvil cells. Mole fractions were determined by isotopic doping of the initial constituents followed by measurement of the equilibrated isotopic content of the decanted samples. Homogenization and de-homogenization of fluids were observed visually for mole fractions of carbon dioxide from 20 to 90%. The recorded pressure-temperature points of homogenization were inverted to give the miscibility surface. The path of the critical curve continues to the highest pressures measured, with no indication of an upper critical end point. For mole fractions of carbon dioxide less than 45% homogenization temperatures decrease sharply at a compositionally-dependent pressure. This is hypothesized to be a result of a rapid change in speciation as the equilibrium between dissolved carbon dioxide and bicarbonate ion shifts towards the latter. Published equations of state give poor representations of the miscibility surface, neither the abrupt behavior due to speciation nor the critical curves being correctly predicted. The experimental constraints provided by the current data should allow useful refinements of equations of state, over a wide PTX range where only extrapolations and molecular dynamic simulations were previously available. Such improved EOS's are prerequisite to better geochemical models for Earth and ocean worlds.

1. INTRODUCTION

Carbon dioxide and water are primary constituents of fluid mixtures in the crust and mantle of Earth as well as in the interiors of several outer solar system icy worlds (McCord et al., 2008; Porco et al., 2006). These fluids are responsible for the transport and concentration of soluble chemical species, mediate the chemical reactivity of rocks (depressing melting points of silicates, and allowing hydration/dehydration and carbonization/decarbonization reactions), alter the rheology of rocks, and are implicated in processes associated with subduction zone tremor (Audet et al., 2010) and deep earthquakes (Abers et al., 2013).

Aqueous solutions of carbon dioxide are particularly important vehicles for carbon transport and likely influence the fate of carbon during subduction (e.g., Hirschmann and Dasgupta (2009); Kelemen and Manning (2015); Sverjensky et al. (2014)). Fluid paths through, along, and out of the slab (see Fig. 1 for subduction geotherms) govern the degree to which carbon is either conducted into the deep mantle or rapidly re-cycled to the surface. Thus, these fluids may be considered gatekeepers in the "carbon cycle."

In the aqueous environments inside large icy worlds the high-pressure solubilities of CO_2 additionally affect the fluid solidus and the evolution of hydrates. Gas hydrates are expected to be major factors in the thermo-chemical evolution of icy moons such as Ganymede or Titan (Sohl et al., 2010).
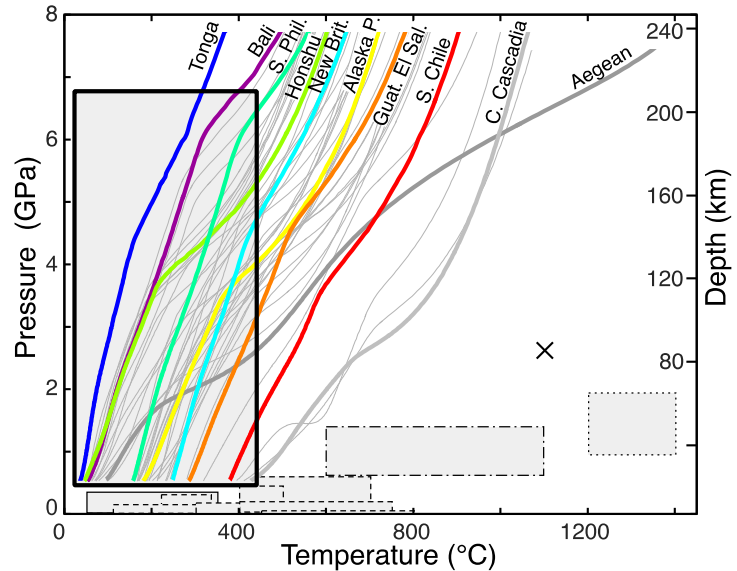

Fig. 1. Temperatures and pressures of the subducting Moho (7 km under the plate interface), as given by model W1300 of Syracuse et al. (2010), with several segments labeled (thicker curves), most not. Overlaid rectangles demark regions in which data exist for the water-carbon dioxide system; of particular note: current study (thicker, solid border); Todheide and Franck (1963), thinner solid border; Aranovich and Newton (1999), dot and dash border; Frost and Wood (1997), dotted border; Eggler et al. (1979), x.

In order to understand processes associated with water-CO_2 fluids, their thermodynamic properties are required within the relevant ranges of pressure, temperature and concentration. Inclusions in diamonds, and in crystals extracted from xenoliths, suggest such fluids extend well into Earth's mantle, to pressures exceeding 10 GPa (Harte, 2010), and that fluid compositions can range from water-rich to CO_2-rich (Andersen and Neumann, 2001). The lowest temperatures at depth, associated with rapid subduction of old oceanic lithosphere, have been estimated by Syracuse et al. (2010) to lie near 400°C at a depth of 240 km and pressure of 8 GPa (Fig. 1). This implied average thermal gradient (1.7 °C/km) is significantly lower than a commonly assumed lower limit for terrestrial metamorphic conditions of 5 °C/km (e.g., Frost and Frost , 2014). Even lower temperatures at pressure pertain to the icy worlds of the outer solar system; for example, the Ganymede ocean-silicate

46 interface near 1 GPa lies within the temperature stability regime of high pressure water ices (Vance et
47 al., 2014).
48
49 Despite the wide applicability of such data, the difficulties associated with studying mixed fluids of
50 water and carbon dioxide are such that almost all previously reported experiments pertain to pressures
51 lower than 1 GPa, most of them below 0.6 GPa (Fig. 1). The only two exceptions are the works of
52 Frost and Wood (1997), limited to temperatures of 1200 to 1400°C, and of Eggler et al. (1979),
53 conducted at 1100°C (see tabulations in Mader, 1991 and in Duan and Zhang, 2006). Furthermore,
54 even well inside the explored regime, at the moderate (~80 MPa) pressures relevant to geothermal
55 engineering significant disagreement on solubilities of water in CO_2 remain (Capobianco et al.,
56 2013).
57
58 The exploration of the fluid-fluid phase diagram at high-pressure has been limited to the works of
59 Todheide and Franck (1963) and Takenouchi and Kennedy (1964) up to ~0.35 GPa. Those studies
60 noted a minimum temperature in the critical curve (saddle point in the solubility surface) at
61 approximately 0.25 GPa, 266°C, and 42 or 30% CO_2, respectively. Above this, the minimum
62 temperature necessary to total miscibility was seen to rise with pressure, but how far it might continue
63 to do so had not been addressed. Models of the mixed fluids during subduction or other deep-Earth
64 processes have therefore relied either on extrapolations of low pressure data or on molecular dynamic
65 simulations.
66
67 Here we present data on the fluid-fluid miscibilities of the water-carbon dioxide system up to a
68 pressure of 7 GPa and temperature of 450°C. Current data, in a range of pressures and temperatures
69 pertinent to conditions in subduction zones, demonstrate that a two-fluid regime extends to the
70 maximum conditions explored. A miscibility surface calculated on the basis of these new data is in
71 substantial conflict with predictions, requiring adjustments of models used in this regime. The current
72 data also indicate the importance of molecular interactions, quite probably including speciation, not
73 contained in most models.
74
75 An equation-of-state (EOS) which correctly reproduces the lower pressure data as well as those of the
76 current study is likely to improve our understanding of fluids within the range of the data, to
77 interpolate well into the economically important, intermediate regime of pressures and, if partially
78 based on theory, to provide a much better grounding for extrapolation to conditions pertinent to
79 higher-temperature rock-fluid interactions.
80
81
82
83 **2. EXPERIMENTAL**
84
85 **2.1 Load preparation**
86 Modified Merrill-Bassett diamond-anvil cells (DACs) were used with rhenium gaskets, the central
87 cavity being lined with gold. Gaskets of hardened Inconel 718, Hasteloy C276 and 316 stainless steel
88 were all found to corrode at the conditions of these experiments. Carbon dioxide, specified as
89 99.995% pure, was obtained from Praxair. For the purpose of determining the ratio of water to carbon
90 dioxide loaded into the DACs (see below, section 2.4) water was usually supplied as a dilute (0.055
91 mol-kg^{-1}) solution of sodium bicarbonate. When loading, the DAC was first immersed in the solution

92 and a partial vacuum briefly drawn. Release back to atmospheric pressure resulted in a load
93 consisting of solution (without alteration of concentration) and a bubble of air. The cells were sealed
94 and transferred to a pressure vessel. Liquid CO_2 at 10°C and 58 bar was admitted into the pressure
95 vessel. The immersed DACs were briefly re-opened to allow liquid CO_2 to displace the air, and then
96 re-sealed.
97
98 When the cell containing solution and an air bubble is first dried, bicarbonate salt can accumulate
99 around the exteriors of the diamonds and is probably concentrated at the join of diamond and gasket,
100 drawn in by surface tension. Opening such a load to the CO_2 can result in an unknown, but
101 significant, quantity of salt crystals being drawn into the cell. Thus, between the initial loading of the
102 solution and the subsequent loading of CO_2, the cell was dried under vacuum, washed in 0.2 mol-kg^{-1}
103 HCl during which time a vacuum was repeatedly drawn on the solution, again dried under vacuum,
104 then placed in an ultrasonic bath of de-ionized water for an hour. Additionally, before loading, any
105 fracture found in the indented rhenium gasket along the diamond pavilion was filled with gold to
106 avoid it becoming an unintended reservoir of material.
107

2.2 Measuring pressure and temperature

108
109 The DAC was placed in an oven with fore and aft optical access. Pressure was determined with a
110 precision of better than 0.1 GPa (rms scatter of 0.05 GPa) from the Raman spectra of one or more
111 crystals of cubic boron nitride placed inside the DAC (Abramson, 2016), stimulated with 20mW of
112 488 nm laser light (Ar$^+$). The back-scattered radiation was collected by a microscope objective of
113 0.28 numerical aperture and 33.5 mm working distance, and dispersed by a 300 mm monochromator
114 with 1800 lines/mm grating. Spectra were typically acquired over an interval of 30 s. Temperature
115 was monitored with type K thermocouples attached near the diamond culets. At the melting point of
116 lead (Pb), 327.45°C (McLaren and Murdock, 1960), the reading was off by 1.5 °C, presumably due to
117 gradients through the cell. Sample temperatures were corrected, assuming the difference between the
118 thermocouple reading and sample temperature to be proportional to the difference from ambient
119 temperature. The maximum correction is less than 2°C.
120

2.3 Determination of homogenization

121
122 Transitions between a homogeneous and a mixed fluid were determined visually. The contents of the
123 DAC were illuminated, with transmitted
124 light imaged onto a CCD camera through the
125 same lens as used to collect Raman scatter
126 followed by a 50% reflectance pellicle
127 beamsplitter. A long-pass optical filter
128 between the (incandescent) light and the cell
129 allowed the cell to be observed at the same
130 time spectra were being taken.
131 At a given pressure, temperature was first
132 raised until the load was seen to be
133 homogeneous, then lowered until the re-
134 appearance of a second phase. These
135 temperatures of transition were recorded, the
136 pressure again raised, and the process
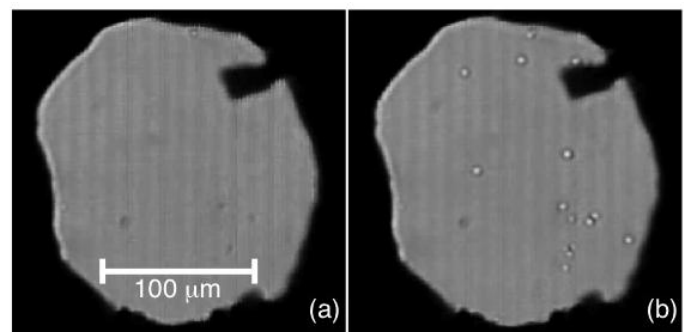137 repeated. The exact temperature of

Fig. 2. De-homogenization at 265°C, 2.7 GPa and X_{CO2}=19%. (a) homogeneous fluid; (b) less than 1°C below the temperature of de-homogenization. The image on the CCD is deliberately de-focused to enhance the contrast between bubbles of minority phase and the bulk fluid. Here is a video of this process*[link to movie 1]*.

138 homogenization can be difficult to determine, particularly if the minority phase is adjacent to (and
139 partially obscured by) the gasket. For most loads the de-homogenization was far more obvious,
140 manifested by the sudden appearance of many small bubbles of minority phase distributed throughout
141 the load (Fig. 2).
142
143 The two types of measurement produced results identical within the expected uncertainties of
144 pressure and temperature; no metastability with respect to de-homogenization (into two fluids) was
145 ever observed. De-homogenization of loads with high X_{CO2} (e.g., 90%) proved more difficult to
146 observe as the minority, aqueous fluid, phase tends to wet any pieces of debris on the diamond
147 surfaces rather than produce obvious bubbles. Analogous problems in observation of small amounts
148 of aqueous fluid have been remarked in experiments which involved synthetic inclusions (e.g.,
149 Bodnar et al., 1985; Sterner and Bodnar, 1991) homogenizing into a vapor phase. None-the-less, the
150 reproducibility of the measurements and, for the 90% load, the straight line paralleling other data,
151 demonstrate that the points of

152 homogenization are correctly determined. For
153 measurements at lower X_{CO2}, the greatest
154 error in this regard appears to be a result of
155 pressure drift between the moment the
156 transition is observed and the end of the
157 pressure measurement; in the absence of
158 pressure drift, the temperatures of transition
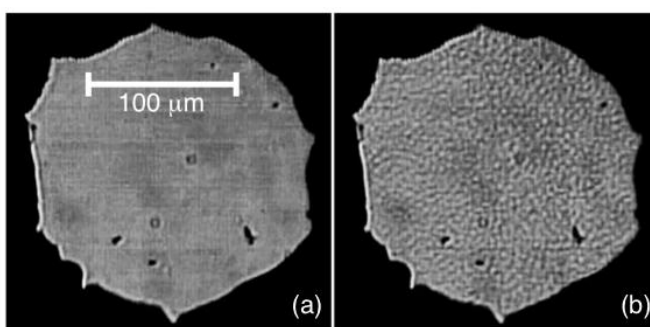159 could be reproducibly measured to 0.1°C .
160

Fig. 3. Critical opalescence at 373°C, 3.9 GPa, and X_{CO2}=57%.
(a) the homogeneous fluid just above the critical temperature;
(b) at the critical temperature. The mottling is on a scale of ~3
μm and could be seen to shimmer. Edge sharpening was
applied identically to both images. Persistent dark spots are
pieces of spalled gasket. Here is a video of de-homogenization
on the critical curve*[link to movie 2]*.

161 Although we did not specifically seek the
162 exact critical conditions for any load, several
163 examples of critical opalescence were
164 observed (Fig. 3). Proximity to the critical
165 curve was also evidenced by the temporal
166 behavior of the fluids on a coarser scale, as
167 the regions of different composition move,
168 dissolve and re-appear rapidly.
169
170
171 **2.4 Measuring mole fractions**
172   At sufficiently high pressures and temperatures (e.g., 0.2 GPa, 300°C) bulk homogeneous CO_2-H_2O
173 solutions might be loaded into the DAC, as was done with the system N_2-H_2O (Costantino and Rice,
174 1991; van Hinsberg et al., 1993). However, due to the cost of the required machinery, concerns of
175 safety, and the extremely corrosive properties of CO_2-H_2O solutions, it is desirable to load at lower
176 pressures and temperatures. This then requires a method of determining the resultant mole fractions
177 of the two, immiscible and separately loaded, components. Approximate values can be estimated by
178 visual observation, but we wished to develop a method capable of greater accuracy. The method
179 chosen was to isotopically dope the water, both with ^{18}O and, through use of 0.055 mol-kg^{-1}
180 NaH^{13}CO$_3$ (0.001 mole NaH^{13}CO$_3$/mole H_2O), ^{13}C. Isotopic transfer to CO_2, measured at the end of
181 the experiment, can then be related to the loaded X_{CO2}.
182

183 In solution, there is rapid exchange between
184 bicarbonate and dissolved CO_2 and thus
185 equilibration of the carbon isotopes.
186 Equilibration of oxygen between water and
187 CO_2 will also be rapid (Poulton and Baldwin,
188 1967), certainly on the time (and length) scale
189 of our experiments, in which both CO_2 and
190 H_2O are in the fluid state at least 5 hours.
191
192 After the observations of homogenization are
193 completed the load is cooled with consequent
194 freezing of both the CO_2 and water; pressure is
195 then brought to roughly 2 GPa. The DAC is
196 placed in an extractor (Fig. 4) which is baked
197 to 160°C under vacuum (<2 mtorr) for 4 hours.

Fig. 4. Diagram of a system for extracting the contents of a DAC into a mass spectrometer. Large crosses denote valves.

198 A typical DAC load contains approximately
199 10-100 nmole of analyte, making a thorough de-gassing of the DAC and extractor (fitted with Viton
200 o-ring seals) imperative. Inside the extractor, and after cooling to room temperature, the cell is
201 opened by a wrench on a rotary feedthrough. The gases from the cell expand into an evacuated tube
202 of 316 stainless steel with 4.5 mm ID, and are rapidly trapped in a U bend immersed in liquid
203 nitrogen. The tube is then swept with a flow of He and the nitrogen replaced with an alcohol/$CO_2(s)$
204 slush, allowing the extracted CO_2 to sublime while retaining the water as a solid. The He flow is
205 directed into a mass spectrometer. Analysis of the DAC loads was performed with a Thermo Finnigan
206 MAT 253 continuous flow, isotope ratio, mass spectrometer.
207
208 *2.4.1 Composition of initial fluids*
209 Isotopically enriched water (with a stated 1.48 mole% [18]O) and bicarbonate (99%[13]C) were purchased
210 from Icon Isotopes. In order to determine the [18]O and [17]O content of the purchased enriched water, a
211 sample was diluted with a laboratory standard deionized water of a known isotopic composition
212 ($\delta^{18}O$= -10.55 VSMOW; $\delta^{17}O$= -5.55 VSMOW) to give a [18]O content of about $\delta^{18}O$= +40 VSMOW.
213 One gram of the diluted sample was then allowed to equilibrate at 24°C with 11 ml of gaseous CO_2
214 (at 1 bar) of known isotopic content. A sample of the gas was then extracted and analyzed. Adjusting
215 for the additional oxygen from the CO_2, and using equilibrium fractionation values for the $CO_2(g)$-
216 $H_2O(l)$ equilibrium of α_{18}=1.041 and α_{17}=1.021 (Barkan and Luz, 2012), the isotopic content of the
217 purchased water was calculated to be 1.47% [18]O and 0.095% [17]O.
218
219 The DAC was loaded with a solution made by dilution of the enriched water (with de-ionized tap
220 water) to 0.404% [18]O (and 0.046% [17]O) and addition of bicarbonate to 0.055 mol-kg^{-1}. The liquid
221 carbon dioxide was derived from a petrochemical source with $\delta^{13}C$= -36.25 (VPDB) and $\delta^{18}O$=
222 +10.72 (VSMOW).
223
224 *2.4.2 Consideration of isotopic fractionation*
225 In the case of carbon, there is no significant chemical fractionation, as virtually all is released as
226 carbon dioxide. For oxygen, we must consider the possibility of a significant shift from the presumed
227 "random" distribution between CO_2 and water due to the greater affinity of [18]O for the former. At 1
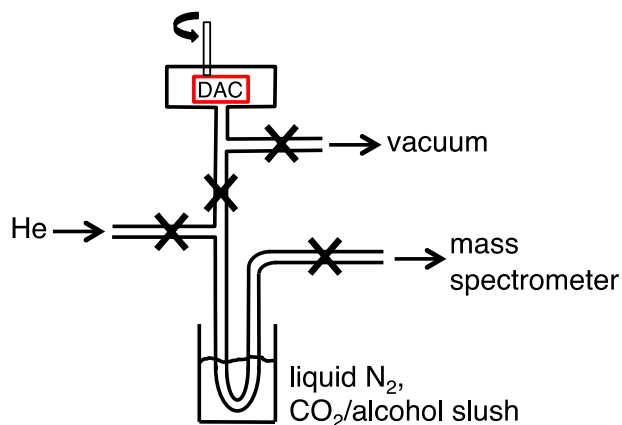228 bar the fractionation factor between gaseous CO_2 and liquid water is 1.041 (41 ppt) at 21°C and it

229 decreases with increasing temperature (Truesdell, 1974) to 8.5 ppt at 450°C; fractionation between
230 liquid CO_2 and water is the same to within 1 ppt (Rosenbaum, 1993) and those between water and
231 either the carbonate or bicarbonate ions are smaller (Beck et al., 2005). All these cited equilibria were
232 measured at 1 bar and little has been written about the effects of pressure. It has been reported that
233 application of 2 GPa pressure on the system of $CaCO_3$ and water (at 500°C) produced no change in
234 the ^{18}O fractionation factor above the measurement uncertainty of 0.2 ppt (Clayton et al., 1975).
235 Evaluation of this equilibrium at the maximum pressure of our current study (and room temperature,
236 for which the effect, proportional to $1/T$, is greatest) indicates that this upper limit would correspond
237 to a maximum shift of <2 ppt, about an order of magnitude less than the effects of temperature, so we
238 may assume the effect of pressure to be relatively small. Considering both pressure and temperature
239 effects, it is therefore assumed that the (unknown) fractionation will not exceed several tens of ppt.
240
241 In order to obviate the effects of fractionation we used amounts of doping far in excess of these
242 variations. The contribution to the uncertainty of the fractionation factor is greatest at low X_{CO2},
243 where the value is maximally controlled by equilibration with the majority water present. For a load
244 with $X_{CO2}=20\%$, an uncertainty of as much as 40 ppt in the fractionation factor (assumed due mostly
245 to a lack of knowledge of the final temperature of equilibration) would lead to an error of 3% in
246 calculated concentration. An error of as much as 40 ppt, however, is improbable as we may
247 reasonably presume that the final distribution of isotopes is not governed by the highest temperature
248 achieved in the experiments. Rather, we expect that equilibration is locked in as the cell load
249 solidifies upon cooling. Since we lower the pressure before the 160°C bake-out, the relevant
250 temperature will be somewhere between the liquidus and solidus of CO_2-saturated water around 2
251 GPa, thus less than 100°C. For our calculations we use the room temperature value for CO_2 over
252 liquid water as the fractionation factor. The fractionation of ^{17}O between CO_2 and water was assumed
253 to be half that between ^{18}O and water (Craig, 1957; Barkan and Luz, 2012). The adequacy of the
254 foregoing assumptions is borne out by the experimental results (see section 2.4.4).
255
256 *2.4.3 Calculation of mole fractions*
257 Given the known, initial isotopic compositions of both the aqueous solution and the liquid carbon
258 dioxide, the fractional amounts $^{13}C/C_{total}$, $^{17}O/O_{total}$ and $^{18}O/O_{total}$ in the resulting, equilibrated CO_2
259 (P_{13}, P_{17} and P_{18}, respectively) could be calculated for any assumed mole fraction in a DAC load.
260
261 In turn, these fractional amounts allow calculation of the expected ratio of the ion current at 45 amu
262 to that at 44 amu as:
263
264 $$R_{45/44} = [P_{13}(1-P_{18}-P_{17})^2 + 2(1-P_{13})(1-P_{18}-P_{17})P_{17}] / [(1-P_{13})(1-P_{18}-P_{17})^2] \qquad (1a)$$
265
266 and that of 46 to 44 amu as:
267
268 $$R_{46/44} = [2(1-P_{13})(1-P_{18}-P_{17})P_{18} + 2P_{13}(1-P_{18}-P_{17})P_{17} + (1-P_{13})P_{17}^2] / [(1-P_{13})(1-P_{18}-P_{17})^2]$$
269 $$(1b)$$
270
271 For each load, $R_{45/44}$ and $R_{46/44}$ were measured and values of X_{CO2} were sought that satisfied each of
272 the two equations, individually. Concurrence of the two values was taken to indicate a probable
273 correct analysis of the DAC contents.
274

275 In order to test our procedure, small aliquots of the working aqueous solution were added to flasks of
276 gaseous carbon dioxide, to produce mole fractions spanning 10 to 85% CO_2. After equilibration for
277 several days, the flasks were placed in liquid nitrogen, then into a slush at -78°C. Samples of the gas,
278 in amounts roughly equivalent to those expected in a typical DAC load (2 μl at 1 bar), were drawn off
279 with a gas-tight syringe. These were then injected into the DAC extraction system through an
280 auxiliary septum and analyzed in the manner described for DAC loads. With good bake-out
281 procedure, the measured X_{CO2} was accurate to better than 1% absolute, for both isotopic gauges.

283 *2.4.4 Precision and accuracy of*
284 *measured mole fractions*
285 Mole fractions of DAC contents
286 determined early on are less reliable
287 than those of the later runs, with results
288 from [18]O typically giving a larger X_{CO2}
289 than from the simultaneous [13]C
290 measurements. Three likely sources of
291 error are 1. oxygen exchange with water
292 (or other sources of oxygen) in the
293 extraction system, which would tend to
294 decrease the amount of [18]O and thus
295 increase the apparent X_{CO2} as indicated
296 by that isotope, 2. aspiration of small
297 crystals of bicarbonate into the load
298 upon re-opening the cell inside the
299 liquid CO_2, which would increase the
300 amount of ^{13}C and thus decrease the
301 apparent X_{CO2} as indicated by ^{13}C, and
302 3. rapid isotope exchange during the few
303 seconds a cell is open inside the liquid
304 CO_2, followed by expulsion of part of
305 the fluids during closure.

Fig. 5. The maximum pressure at which two fluid phases can co-exist is plotted against X_{CO2}, the latter measured by [18]O (*) and [13]C (o) content, with solid and dashed straight line fits to the two, respectively. Mole fractions exhibit a rms deviation of 2% from the lines, and a maximum outlier of 3%. All points with X_{CO2} <40% are plotted; most derive from the later, more fastidious, loading and purging techniques.

307 During the course of the experiments it
308 became apparent that determinations based on [18]O were usually consistent with each other and could
309 provide a smooth miscibility surface, while those based on ^{13}C were more subject to error. Our
310 understanding of the likely sources of errors, and the systematics of the results, indicated that simply
311 rinsing the cell directly after loading with solution was inadequate. Further methods (acid bath,
312 ultrasonification, filling cavities with gold), as described in section 2.1, as well as longer periods of
313 bake-out, were progressively undertaken with the result that the ^{13}C and [18]O measurements converged
314 to a rms deviation of 4% or, barring one outlier, 2.5% (calculated for the last 16 measurements).

316 A better appreciation of the precision, and perhaps accuracy, of the current measurements can be
317 achieved by considering the limiting pressures of immiscibility of those loads with X_{CO2}<40% (see
318 section 3.1). When plotted against X_{CO2} as measured by either [18]O or [13]C (Fig. 5), these pressures can
319 be reasonably fit to straight lines with rms deviation of 2% in X_{CO2}. The best-fit lines for the two
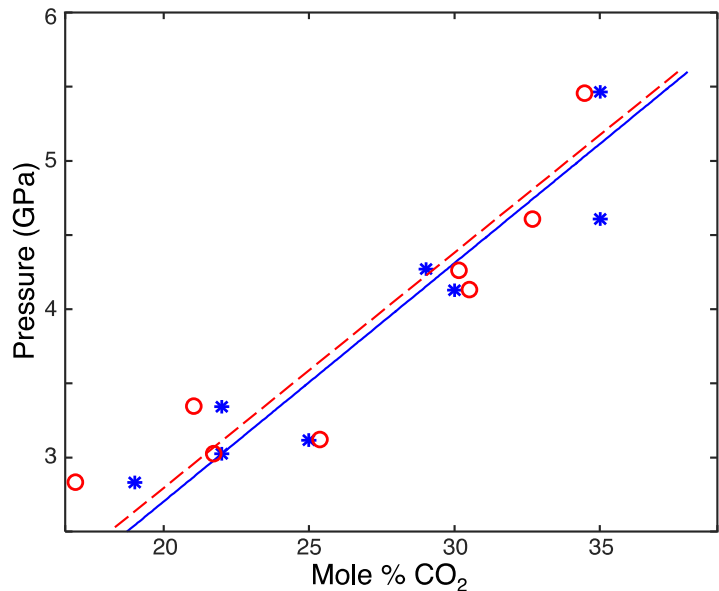320 isotopes differ by less than 0.8% in X_{CO2}.

321 **2.5 Results**
322
323 *2.5.1 Compositions explored*
324 In all we have investigated 30 different DAC loads, 26 of them with isotopic doping (Table I). The
325 loads may be categorized into three types:
326 1. seventeen for which X_{CO2} as measured by ^{13}C and by ^{18}O agree to within 4% (mostly later data)
327   and together define a smooth surface.
328 2. those with ^{18}O a likely close upper bound in X_{CO2} but incompatible ^{13}C results ranging from 4 to
329   27% lower. There are six of these, most acquired before taking steps to reduce ingress of salt dust.
330 3. three sets of data (two from the earliest runs) for which we suspect the ^{18}O to be in serious error,
331   and four without isotopic doping. For these seven sets only the shape and position of the curve is
332   considered of importance. X_{CO2} for the three outlying, doped samples have been estimated from
333   comparison with the other data and are given parenthetically in the table.
334 Tables of the observed points of homogenization are given as Supplementary Data.
335
336 The data sets taken in the absence of isotopic doping, and thus in the absence of added salt, do not
337 demonstrate noticeably different behavior from those with 0.055 mol-kg^{-1} NaHCO$_3$. In particular,
338 three such sets exhibit the same pressure/temperature limit along what has been identified as the
339 critical curve (see section 3.1). In these three, early experiments, one of the cells had the usual
340 rhenium gasket lined with gold, one of rhenium without liner, and another a gasket of Hasteloy C276
341 which suffered increasing corrosion over the course of the measurements. It may be reasonably
342 inferred that the critical limit, and probably the balance of the data, were unaffected by either the
343 deliberately added bicarbonate or any possible products of corrosion.
344
345 In Fig. 6a, pressures and temperatures of homogenization are plotted for 15 compositions, chosen to
346 display the full range of X_{CO2} . Additional data are shown in Fig. 6b, limited to a broad range of X_{CO2}
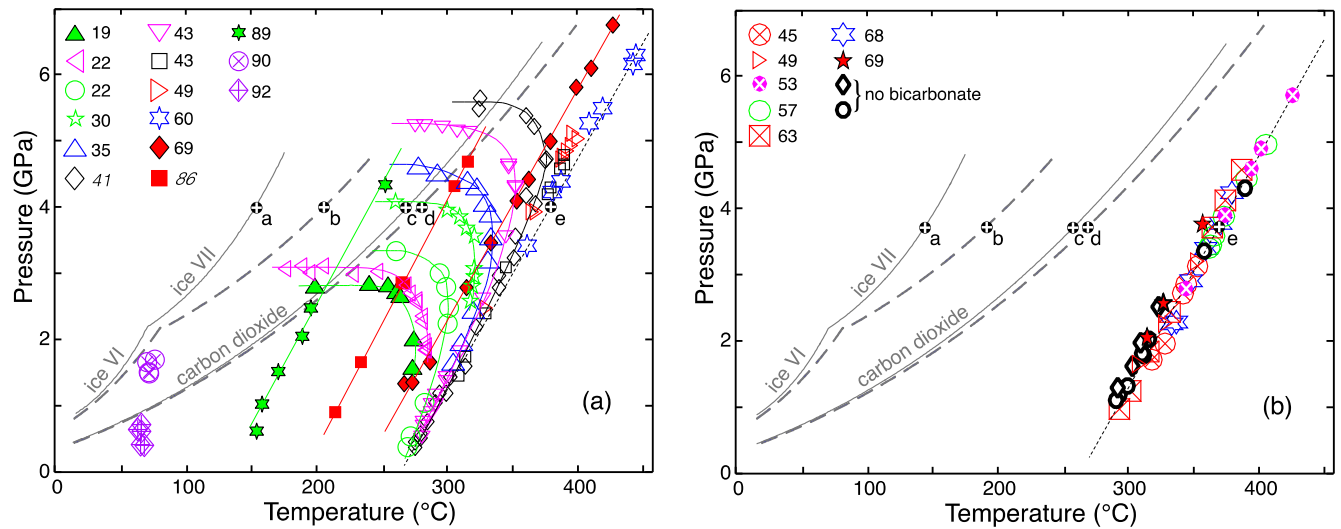347 between 45 and 70%.

Fig. 6. In each panel pressures of homogenization are plotted against temperature. Numbers in the legends give X_{CO2} in mole percent as determined from [18]O content; two italicized numbers give best estimates in the absence of isotopic data. Melting curves of water and CO_2 are given for the pure compounds (long dashed lines; Wagner et al. 1994; Datchi et al., 2000; Abramson, 2016) and saturated solutions (solid lines; Bollengier et al., 2013; Abramson, 2016). Filled circles overlaid with "+" and labeled from "a" to "e" refer to points shown in Fig. 11. The straight lines with short dashes indicate a best fit through points associated with visually observed critical behavior (Eq. 2). (a) Fifteen different DAC loads show the progression from back-hooked curves at low values of X_{CO2} to constant slopes at high values. (b) Traces from nine loads with X_{CO2} between 45 and 70% line up near the pressures and temperatures of the critical curve, evidencing a slow variation of the miscibility surface in the region around the critical concentrations.

348
349 *2.5.2 Temperature-pressure traces*
350 A typical load is initially solid, producing fluid when warmed. As an example, and with reference to
351 Fig. 6a, consider a load with X_{CO2}=19%, starting at room temperature and constrained to warm along
352 a 2.0 GPa isobar (as appropriate for a nearly isochoric sample chamber, pressure increases only
353 modestly with increasing temperature, with larger increases during melting transitions). When a
354 temperature of 65°C is reached the water (ice VI) melts in equilibrium with a eutectic concentration
355 of water and carbon dioxide, achieved by the concomitant dissolution of solid CO_2 (Abramson, 2016).
356 Solid CO_2 continues to dissolve into the aqueous fluid with increasing temperature. At 161°C, which
357 is the melting point of water-saturated CO_2 on the 2.0 GPa isobar, the remaining solid CO_2 melts to
358 produce a second fluid. Further increase in temperature results in the two phases dissolving into each
359 other and finally, at 275°C, a single, homogeneous fluid remains. Repeating the experiment at
360 different starting pressures results in a pressure-temperature curve that defines the surface of
361 miscibility along this single (compositional) isopleth of X_{CO2}=19%. When lowering the temperature,
362 fluid-fluid de-mixing can often be followed into a region in which the fluids are metastable with
363 respect to precipitation of solid CO_2, providing points on the low temperature side of the CO_2 melting
364 line.
365
366
367
368
369
370

3. DISCUSSION

3.1 Observed progressions in the temperature-pressure traces

The lowest pressure of our experiments was 0.4 GPa, slightly higher than the saddle point evident from the data of Todheide and Franck (1963) or Takenouchi and Kennedy (1964); as expected from these previous works, the temperatures of homogenization (T_h) along compositional isopleths initially increase with pressure. In systems with small X_{CO2}, as pressure continues to rise T_h reaches a limiting value and then declines abruptly along a good approximation to an isobar (*e.g.*, 2.8 GPa for X_{CO2} =19%). Exceeding the pressure of that isobar results in an exit from the two-fluid regime. This limiting pressure increases as X_{CO2} increases (Figs. 5 and 6). At the highest concentrations of carbon dioxide the temperature reversal, if it exists, is not observable due to freezing out of $CO_2(s)$.

If instead we were able to increase the CO_2 content along an isobar we would observe first an increasing T_h, followed by a plateau with relatively constant T_h over a broad composition range, and finally a decrease. Thus, the single fluid regime is entered at relatively low temperature for loads of either small (back-hooked traces in Fig. 6a) or large (linear traces) X_{CO2}, while data from loads with X_{CO2} between 45 and 70% lie along substantially the same line (Fig. 6b). Points in this progression for which $(\partial T_h/\partial X_{CO2})_P=0$ define the critical curve. The pressure-temperature coordinates of the critical curve are manifested as the pronounced, high temperature limit of the combined de-mixing curves and are measureable independent of a knowledge of concentrations.

3.2 Miscibility surface

The data can be inverted to define the surface of miscibility $T_h(X_{CO2}, P)$ shown in the contour plot of Fig. 7 (see also the Supplementary Data). Mole fractions were taken as determined by measurements of ^{18}O from data types 1 and 2. The surface was constructed from splines which were required to afford a smooth approximation to the data, including allowance for the P-T traces for which X_{CO2} was not measured but which must fit at some assigned value of composition.

Surfaces drawn from both our new data and previous lower pressure work are shown together in Fig. 8 with a logarithmic pressure scale. Overall, as pressure rises, the maximum surface temperature is seen first to descend from the critical point of pure water to the previously noted saddle point and then to
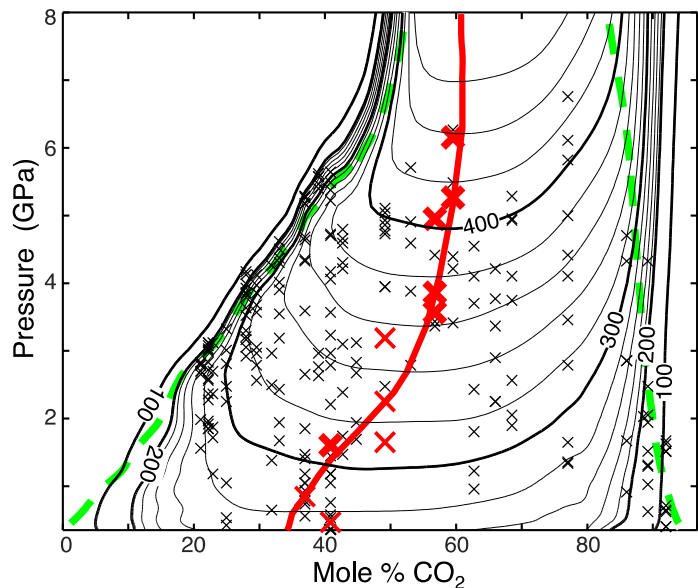

Fig. 7. Temperature contours of the calculated miscibility surface are plotted against mole fraction carbon dioxide and pressure. An estimate of the critical curve is given by the thick (red) curve. The dashed (green) curves indicate where the surface crosses the melting temperature of water-saturated carbon dioxide. Locations of our data are denoted by small (black) crosses. Larger (red) crosses denote points at which near-critical behavior was observed with the thicker of these pertaining to critical opalescence (Fig. 3) and the thinner to rapid movement and collapse of larger bubbles.

417 rise again, while X_{CO2} consistently
418 increases. It is indicative of the rapidly
419 varying nature of the fluids that a mixture
420 with X_{CO2}=30%, when held at 300°C, is
421 homogeneous at 10 MPa, but then with
422 increasing pressure de-mixes at 15 MPa, re-
423 homogenizes at 60 MPa, de-mixes again at
424 1.4 GPa and once again homogenizes at 4.0
425 GPa, just before the precipitation of solid
426 CO_2.
427
428 *3.2.1 Speciation*
429 In Fig. 7 and the upper part of Fig. 8, the
430 edge of closely space contours on the side
431 of low X_{CO2} corresponds to those sections of
432 the P-T traces which are seen to hook back
433 to lower temperatures. This rapid plunge in
434 the temperature necessary for miscibility is
435 believed to indicate a correspondingly rapid
436 change of chemistry with the increased
437 pressure. Facq et al. (2014) explored the
438 speciation of aqueous CO_2 and suggested
439 that CO_2 dissolved in water is mostly in the
440 form of molecular CO_2 at our lower
441 pressures but, as pressure is raised,
442 dissociates to produce bicarbonate. For
443 X_{CO2} =20%, and 200°C, calculation based
444 on thermodynamic quantities given by Facq
445 et al. indicates that the fraction of the CO_2
446 in bicarbonate form should rise from less

Fig. 8. Temperature contours (°C) of the calculated miscibility surface are plotted against mole fraction carbon dioxide and pressure; the thicker (red) line indicates the critical curve. Contours (black) below 0.35 GPa follow the data of Todheide and Franck (1963) with the critical curve given as the thick, solid (magenta) line. Dashed (blue) contours and italicized temperatures represent some of the data of Takenouchi and Kennedy (1964) with their estimate of the critical curve given by the thick, dashed (blue) line. Asterisks mark the saddle point as determined by these two previous studies.

447 than 2% at a pressure of 2 GPa to 45% at 4 GPa. Although the calculation assumes dilute solution
448 properties and may not be entirely appropriate for our more concentrated solutions, this predicted
449 range of the transition to disassociated species brackets the observed homogenization at 2.8 GPa.
450
451 If the observed, pressure-enhanced solubility of carbon dioxide in water is in fact due to the formation
452 of bicarbonate, an accurate thermodynamic description of the system requires that such speciation be
453 taken into account, and simpler models are unlikely to be satisfactory across multiple regions of
454 different speciation. It is also reasonable to suppose that with a rise in X_{CO2} there will be a
455 concomitant drop in the dielectric constant of the fluid so that dissolved, neutral CO_2 will become
456 more stable with respect to its ionized species, and increases in pressure will be less effective in
457 bringing about homogenization. For this reason, at mole fractions X_{CO2}> 40%, where data are not
458 available along this edge, we have chosen to draw the contours to more closely parallel the pressure
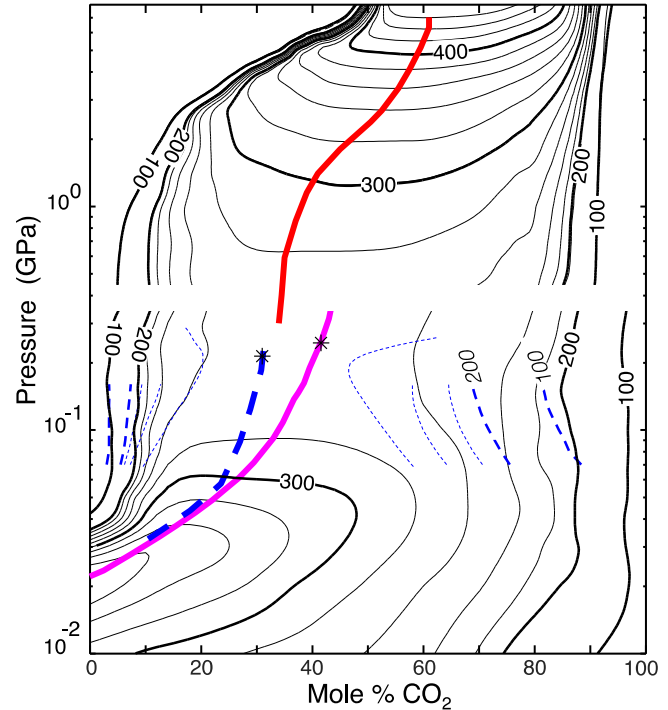459 axis.
460
461
462

463 *3.2.2. Comparison of overlapping data sets*
464 In constructing the miscibility surface, the data of Todheide and Franck (1963) taken at 0.35 GPa
465 were used for values of X_{CO2} less than 80%, in which range their data were not inconsistent with ours.
466 At higher X_{CO2} the two data sets are not in agreement. Similarly, the studies of Todheide and Franck
467 (1963) are in reasonable agreement with those of Takenouchi and Kennedy (1964) for lower X_{CO2},
468 but the two differ significantly above approximately X_{CO2}=50%. Subsequent work of Mather and
469 Franck (1992) determined homogenization curves with individual loads of constant, known
470 composition (as in this study) in place of sampling the two fluids at a variety of P-T conditions as in
471 the previous two studies. The substantial agreement with the work of Todheide and Franck (1963)
472 was used to argue that their determination of sample contents was correct. A single point at 0.3 GPa,
473 the highest pressure reported by Mather and Franck (1992), did not fit the previous data and was
474 hypothesized to indicate systematic error in the results of Todheide and Franck (1963) at pressures
475 above the saddle point. The only near overlap of any of those high-X_{CO2} data with ours is at our
476 points around 0.4 GPa, 66°C and X_{CO2}= 92%. A short extrapolation from the highest pressure of 0.35
477 GPa in Todheide and Franck (1963) predicts at the same pressure and temperature a fluid with
478 X_{CO2}>98%. The section of pressure-temperature-composition space in which these points occur is at
479 the furthest extent of both experiments, and was covered neither by Takenouchi and Kennedy (1964)
480 nor by Mather and Franck (1992), and the discrepancy remains unresolved. It is notable that, as seen
481 in Fig. 6a, our higher pressure points with similar X_{CO2} (90%) evidence a supercooling (with respect
482 to precipitation of solid CO_2) of at least 50°C, much larger than is typical of pure CO_2; it seems
483 unlikely that this could occur for such small water content as suggested by the data of Todheide and
484 Franck (1963).
485
486 **3.3 Other equations of state**
487 A variety of equations of state for the water-CO_2 system have been proposed in the literature, and are
488 used in various geophysical models. Among the more commonly cited are a modified Redlich-
489 Kwong expression (Kerrick and Jacobs, 1981; Jacobs and Kerrick, 1981), highly parameterized virial
490 expansions fit to combinations of low pressure data and higher pressure simulations (Duan and
491 Zhang, 2006; Zhang and Duan, 2009; Zhang and Duan, 2010), and modified van Laar expressions for
492 excess Gibbs free energy (Aranovitch and Newton, 1999); Holland and Powell, 2003).

Miscibility surfaces as predicted by these representations were tested against our data. For each EOS, Gibbs free energies were calculated on a grid of P, T and X. At each P and T the method of common tangents (Whitson and Brule, 2000) was used to locate a pair of X_{CO2} in equilibrium (if such existed), one corresponding to a water-rich and the other to a CO_2-rich fluid. The totality of these pairs defines the miscibility surface. Isotherms through the surface (binodal curves) are plotted in Fig. 9 for 400°C and 600°C. At 400°C, these EOS predict lower minimum pressures, and much wider compositional ranges of immiscibility and de-mixing, than observed. Those of Holland and Powell (2003) and of Kerrick and Jacobs (1981), which give a somewhat narrower compositional range of de-mixing, have curves centered at ~30%, comparable to the lower pressure data of Takenouchi and Kennedy (1964) but which fail to move to higher X_{CO2} with higher pressure (and temperature). Of the EOS tested, the exception is that of Duan and Zhang (2006) (not to be confused with the later Zhang and Duan (2009)) which errs in the contrary direction and, at 400°C, predicts complete miscibility within its claimed limits of validity (P<10 GPa). [Note: Holland and Powell (2003) give, and use, two different values for the interaction energy parameter; we have used a_{hc}=10.5, which was optimized specifically for the CO_2-H_2O interaction.] As most of the data available to construct the above EOS were not in the pressure-temperature
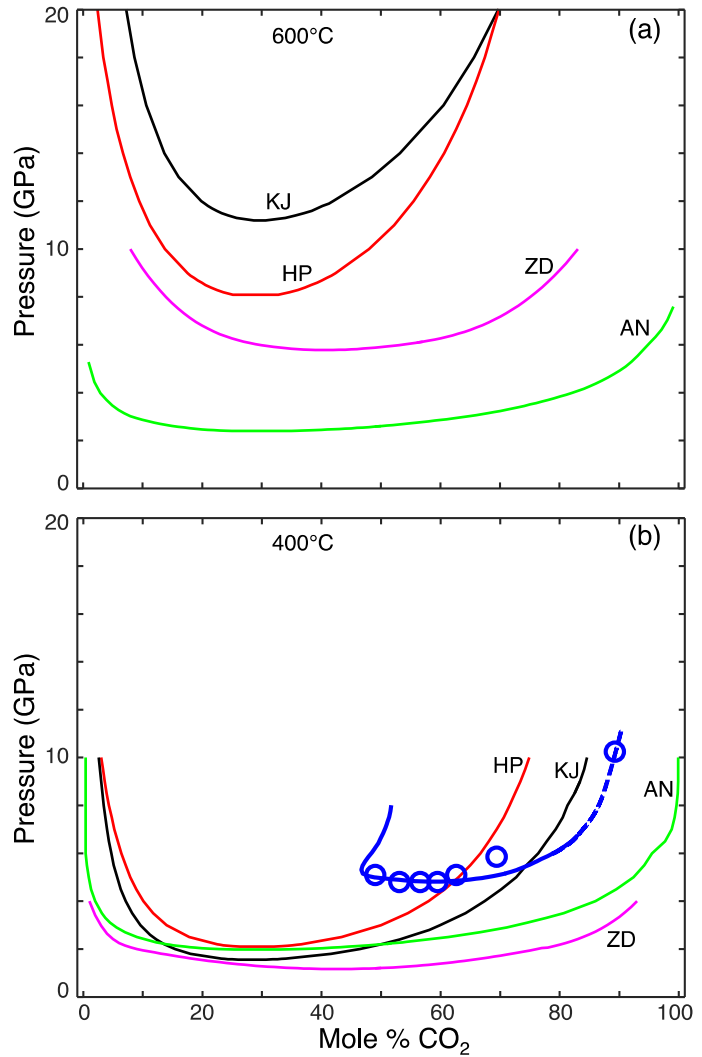

Fig. 9. P-X $_{CO2}$ sections of the miscibility surface at (a) 600°C and (b) 400°C for several different EOS (Holland and Powell, 2003; Kerrick and Jacobs, 1981; Aranovich and Newton, 1999; Zhang and Duan, 2010). The thicker (blue) curve in the lower panel is from our current work (dashed portion extrapolated), with circles marking where seven compositions were seen to de-homogenize with increasing pressure. Below a composition of X_{CO2}=45% no de-mixing occurs at 400°C, at any pressure; this is believed due to a shift in speciation to bicarbonate, a phenomenon not included in any of the models.

regime of the current experiments and, moreover, the prediction of de-mixing is a sensitive test, it is perhaps not surprising that these fail to reproduce measured binodals. Still, the extreme mismatch on the low X_{CO2} side may be due more to a basic failure to account for speciation. If this is the case, it suggests that these EOS are not suitable as the basis of more complex models of COH fluids, including their saline solutions.

539

3.4 Critical curve

The CO_2/H_2O system exhibits type III phase behavior (van Konynenburg and Scott, 1980) and so has two sections of critical curve. One section is extremely limited and pertains to a gas and a fluid, both of which closely approximate pure CO_2, in equilibrium with an aqueous fluid; it starts at the critical point of CO_2 (31.0°C, 7.38 MPa), terminates in an upper critical endpoint at 31.5°C and 7.411 MPa (Wendland et al., 1999), and is of no concern here. The more interesting section starts at the critical point of pure water (374°C, 22 MPa) and continues beyond the highest pressures and temperatures of this study.

In Fig. 10 our data are plotted now on a semilogarithmic pressure scale. The line of turning points which indicates the critical curve is seen to fair nicely into critical points as tabulated by Todheide and Franck (1963). Points where critical or near-critical behavior were observed (Fig. 3) are indicated (see also, Fig. 7). Pressures and temperatures along the critical curve are well determined; a straight line fit to these observed points yields the equation:

$$P_{crit}=3.5 \times 10^{-2}\, T_{crit} - 9.2$$
(2)

with maximum deviation of 0.15 GPa. The surface does not peak sharply in X_{CO_2}, being very broad, and so critical concentrations as determined by P-T-X data are not as closely constrained. While the fitted surface is consistent with the observations of critical phenomena, the precise concentrations may be somewhat better determined by the latter.

In Fig. 9, the minimum pressure of each binodal defines a critical P-T-X point of the associated EOS. Such calculations can be repeated at different temperatures and the critical curves thus mapped out. These curves have been calculated for literature EOS and their P-T traces are depicted in Fig. 10. As with the binodals, most EOS predict much higher temperatures than determined experimentally. The exceptions are the EOS of Duan and Zhang (2006) which necessitates an upper critical endpoint at some temperature below its limit of 400°C (and a corresponding pressure below 7
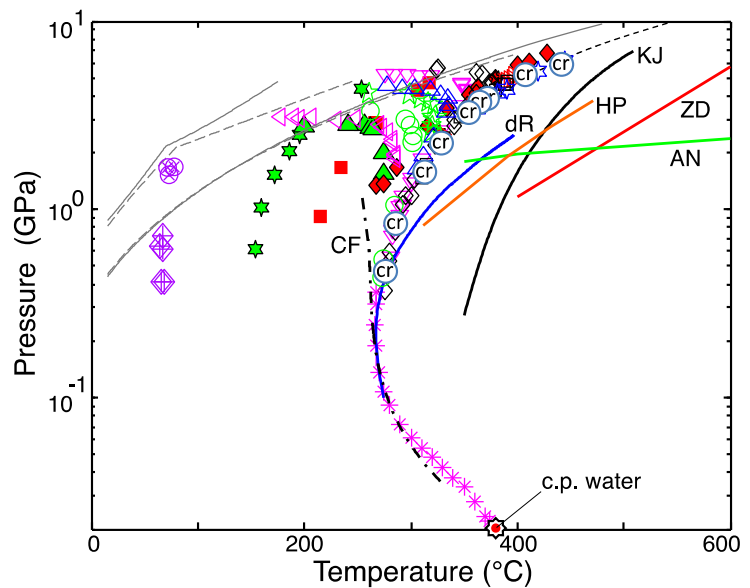

Fig. 10. Points of homogenization as in Fig. 6a, plotted on a semilogarithmic pressure scale to better display the critical points tabulated in Todheide and Franck (1963) (*). Symbols found in Fig. 6a retain their previous meanings. Points at which (near)-critical behavior was seen are denoted by circles containing the letters "cr." Both the (water-saturated) CO_2 freezing curve and the fitted critical curve are continued to 10 GPa. Also shown are critical curves given by various EOS (Holland and Powell, 2003; Kerrick and Jacobs, 1981; Aranovich and Newton, 1999; Zhang and Duan, 2010; dos Ramos et al., 2007; Christoforakos and Franck, 1986). For clarity the last curve is drawn in alternating dots and dashes. The critical point of pure water (22 MPa and 374°C) is indicated.

585   GPa, where the critical curve would intersect the three-phase $CO_2(s)$-L_1-L_2 line), and also of
586   Christoforakos and Franck (1986) which deviates to lower temperatures. Both this last EOS and one
587   derived by dos Ramos et al. (2007) from Statistical Associating Fluid Theory (SAFT) were forced to
588   conform to the experimentally determined values near the minimum in T_h, but diverge rapidly from
589   measurements once beyond the region of previously available data.
590
591   **3.5 Adding solids to the phase diagram**
592   Superimposed on the surface in Fig. 7 is the thermodynamic limit of the two-fluid regime due to the
593   freezing of CO_2 (however, a homogeneous fluid, metastable to the precipitation of $CO_2(s)$, has been
594   observed). At low X_{CO2} the temperature limit is given by the freezing of water-saturated CO_2 while
595   on the opposite end, depending on the exact value of X_{CO2}, the limit falls between that temperature
596   and the slightly higher freezing temperature of pure CO_2. With further pressure increase, the fluid-
597   fluid critical temperature might fall below the freezing point of water-saturated CO_2, which would
598   result in an upper critical endpoint. Above that pressure, only ice and/or a single fluid would exist.
599   However, this has not been observed and, as shown in Fig. 6, the freezing line of water-saturated CO_2
600   trends away from that of pure CO_2 with increasing pressure, which slows its approach to the critical
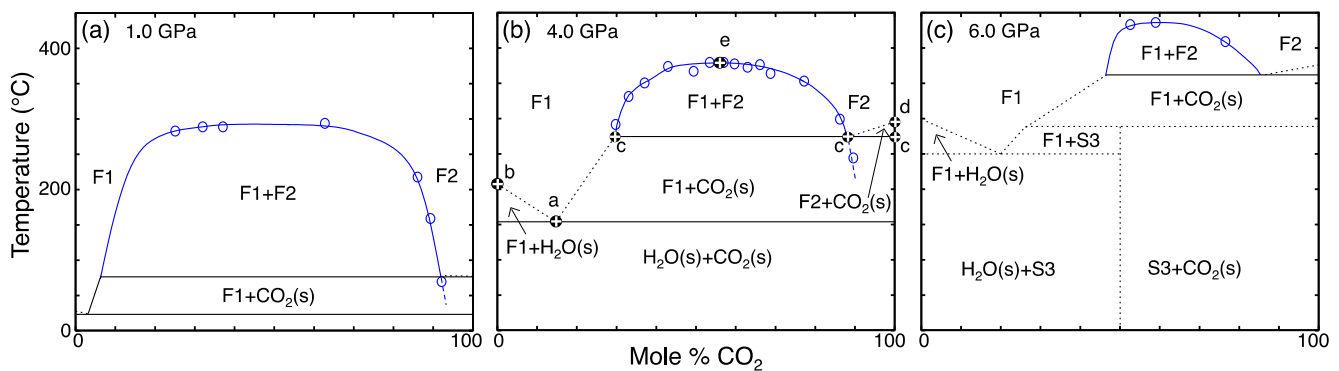601   curve.

Fig. 11. T-X_{CO2} cross-sections at pressures of 1.0, 4.0 and 6.0 GPa. Regions of stability of two different fluids, solid water and solid CO_2 are shown. Dashed extensions of the fluid-fluid equilibrium surface indicate metastabilities. Open circles indicate temperatures of homogenization for various sample loads. In the center (panel b), the labels a, b, c, d and e refer, respectively, to the F1-$H_2O(s)$-$CO_2(s)$ eutectic equilibrium, the melting point of pure water, the F1-F2-$CO_2(s)$ equilibrium, the melting point of pure CO_2 (which in this panel is exaggerated by 10°C in order better to reveal the small region of under-saturated CO_2 fluid), and the critical point at this pressure; these labels correspond to those in Fig. 6. X_{CO2} for point "a" has not been measured, nor have those phase boundaries denoted by dotted lines. A third phase recently reported by Wang et al. (2016), and identified by those authors as β-H_2CO_3, is shown at 6.0 GPa as S3; only the fluid-fluid region of this diagram has been experimentally determined in this current work, while the boundaries of the solid phases are speculative.

602   T-X cross-sections of the phase diagram are shown in Fig. 11 at three different isobars. Labeled
603   points in the middle panel are also indicated in Fig. 6. The temperatures of the eutectic (points on the
604   F1-$H_2O(s)$-$CO_2(s)$ line, here labeled "a") have been measured (Abramson, 2016) however their X_{CO2}
605   are unknown; values of X_{CO2} for the points and, the lines leading to them from higher and lower
606   X_{CO2}, are approximate. As pressure increases it can be seen in the diagrams that the region of fluid-
607   fluid immiscibility narrows, while its center moves to higher X_{CO2}.
608
609   **3.6 Densities of de-mixed fluids**
610   Fluid densities are estimated using the known equations of state of the pure end-members (Abramson
611   and Brown, 2004; Giordano et al., 2006), assuming that the volumes of mixing are negligible.

612 Measurements indicate a maximum excess volume of 4% at 0.6 GPa (Sterner and Bodnar, 1991), and
613 MD simulations (Brodholt and Wood, 1993) suggest it to be less than 1% above 1 GPa.
614
615 In Fig. 12, density contours are
616 superimposed on the miscibility surface.
617 These contours, evaluated at their
618 intersection with a given isotherm and
619 isobar of miscibility, can be used to
620 determine differences in density between
621 two ex-solved phases. For example, at 6
622 GPa and 400°C, the ex-solved phases
623 (with X_{CO2} about 50% and 80%) differ by
624 about 0.1 g-cm^{-3}, and at 1 GPa and 200°C
625 (with X_{CO2} about 10% and 85%) by about
626 0.2 g-cm^{-3}.
627
628 Density differences between immiscible
629 fluids have the potential to drive large
630 scale chemical fractionation of fluids in
631 subduction zones. The dynamics of this
632 process will require, in addition,
633 consideration of pore sizes, fluid

Fig. 12. Density contours (g-cm^{-3}) of the homogeneous fluid are overplotted as (red) dashed curves on the miscibility surface.

634 viscosities, and wetting behavior (Corey, 2003). Whether fluid inclusions in rocks retain a record of
635 such two-phase separation remains unknown.
636
637 **3.7 Implications for planetary interiors**
638 This study provides essential experimental constraints on the chemical behavior of the pure C-O-H
639 fluid under planetary conditions of pressure and temperature. Results highlight a need to improve the
640 thermodynamic description of this important mixture. An understanding of the complex geochemical
641 and geophysical processes that ultimately control the habitability of Earth and the evolution of planets
642 requires use of accurate thermodynamic properties for all constituents under the relevant conditions
643 of pressure and temperature. Whether carbon is retained in subducting slabs or exchanged through
644 volcanic emissions with the atmosphere depends on complex multicomponent chemical reactions
645 between fluids and rock, as well as mass transport and chemical fractionation within a permeable
646 rock matrix. Such physical and chemical complexity also figures into the evolution of the outer solar
647 system ocean worlds (including Europa, Ganymede, and Titan) that likely have significant reservoirs
648 of CO_2.
649
650 We find that, in a regime of pressures and temperatures associated with both terrestrial subduction
651 zones and ocean worlds of the outer solar system, the pure water-carbon dioxide miscibility surface is
652 not well predicted by any of the standard thermodynamic descriptions. A common idea that C-O-H
653 fluids are homogeneous at all temperatures above about 350°C in "much of the crust and all of the
654 mantle" (Manning and Shock, 2013) is not supported by the current experiments. A more
655 consequential disparity may underlie the argument, given by Ague and Nicolescu (2014), that more
656 CO_2 is lost from subducted carbonates in the Cycladic subduction complex (Greece) than can be
657 explained by geochemical modeling. Thus, in a regime overlapping with planetary conditions,
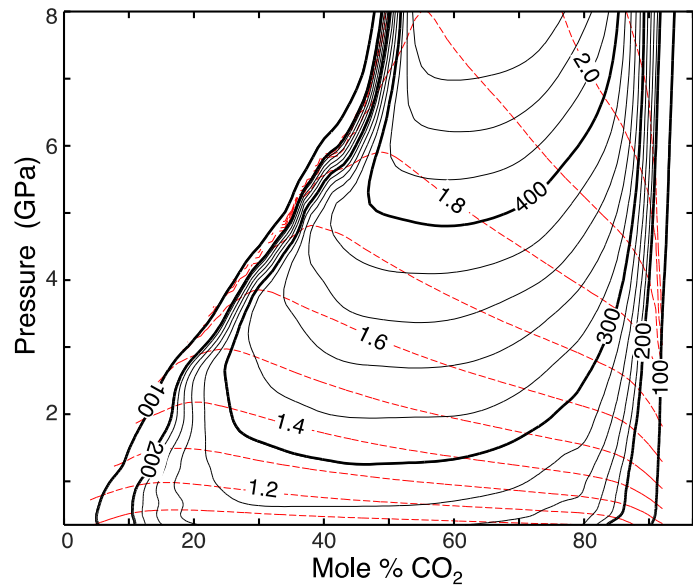
658 petrological predictions remain tenuous using standard thermodynamic models for complex rock-
659 fluid systems.
660
661 We emphasize the need to extend thermodynamic theories beyond current arbitrary and simple
662 implementations. An approach based on end-members with a single mixing parameter is not able to
663 provide a satisfactory description over an extended range of pressure, temperature and composition.
664 Many of the numerical formulations for end-member equations of state are essentially truncated or
665 power law expansions of a thermodynamic potential. By design, these can accurately fit data over
666 some limited range but demonstrably fail in extrapolation to the newly investigated conditions.
667
668 Our results strongly suggest that ionic speciation makes a major contribution to C-O-H energetics at
669 pressures beyond 1 GPa. Since, as noted by Benezeth et al. (2013) "the ionization of carbonic acid is
670 probably among the most important reactions in natural geothermal fluids", it is essential that changes
671 in thermodynamic behavior at high pressure be correctly described. This is particularly challenging
672 since a successful theory must accurately describe the behavior of dilute (a focus of electrolytic
673 solution theory) and carbon-concentrated solutions. Any evaluation of carbon flux (Kelemen and
674 Manning, 2015), or of the solubilities of rocks in metamorphic fluids (Galvez *et al.*, 2015), requires
675 knowledge of the dielectric constant of the solvent. Methods of evaluation typically use the end-
676 member values as input to a variety of mixing schemes. None of these schemes, however, takes into
677 account the possible bulk changes in solvent (CO_2) speciation. Approximations of the dielectric
678 constant assuming both water and CO_2 to exist entirely as the electrically neutral species, as per the
679 methods of Looyenga (1965), will not give correct results for a fluid in which much of the CO_2 exists
680 in an ionic form. Likewise, molecular dynamic modelling has been used to calculate the dielectric
681 constant of water-CO_2 mixtures for purposes of geochemical computation (Mountain and Harvey,
682 2015), but just as for MD calculations of the EOS of these fluids (*e.g.*, Duan and Zhang, 2006;
683 Brodholdt and Wood, 1993) there is the underlying assumption that the CO_2 exists as the neutral
684 molecule. Solubility calculations such as those of Galvez *et al.* (2015) will need to be re-visited if a
685 substantial fraction of the dissolved CO_2 is ionic in nature.
686
687 Of course, while an understanding of the thermodynamics of the water-carbon dioxide binary is the
688 basis for modelling the dissolution of salts into these fluids, the addition of salts, in turn, can be
689 expected to alter the phase equilibria. These effects, while not yet measured at the conditions of the
690 current experiments, can be expected to be large, as seen at lower pressures (Gehrig et al., 1986).
691 Still, trends associated with the binary are likely to persist in more complex chemical systems.
692
693 **4. CONCLUSIONS**
694
695 We document successful use of isotopic doping as a method to accurately determine fluid mole
696 fractions of diamond-anvil cell loads. Fluid-fluid phase equilibria in the water-carbon dioxide binary
697 have been measured to pressures of 7 GPa and temperatures of 450°C, extending our knowledge of
698 this system to Earth mantle conditions, particularly those expected in rapidly subducting slabs.
699
700 A miscibility surface has been constructed and the critical curve was determined. Systems with mole
701 fractions of CO_2 less than roughly 45% exhibit a maximum pressure above which the components are
702 infinitely miscible; this maximum increases with pressure and is likely due to a shift in speciation of
703 CO_2 favoring the formation of bicarbonate. As well, the concentration along the critical curve shifts

with pressure to higher fractions of CO_2, perhaps for the same reason. To the highest pressures achieved in this study fluid-fluid immiscibility persists, and any imminent critical endpoint is not evident in the data; at the higher pressures, the rate at which the liquidus approaches the critical curve diminishes.

Since water and carbon dioxide are ubiquitous planetary components, nearly all geochemical models include descriptions of their combined equation of state in order to calculate equilibrium behavior of complex mixtures. No EOS tested against the observations reported here is successful. Thus, it would appear that model predictions are not robust in this regime of P and T. Better parameterizations and consideration of speciation are needed.

References

Abers G. A., Nakajima J., van Keken P. E., Kita S. and Hacker B. R. (2013) Thermal–petrological controls on the location of earthquakes within subducting plates. *Earth Planet. Sci. Lett.* **369-370**, 178-187.

Abramson E. H. and Brown J. M. (2004) Equation of state of water based on speeds of sound measured in the diamond-anvil cell. *Geochim. Cosmochim. Acta* **68**, 1827-1835.

Abramson E. H. (2016) Three-Phase Melting Curves in the Binary System of Carbon Dioxide and Water. *J. Phys.: Conf. Ser. Joint 25th AIRAPT International Conference / EHPRG Meeting on High Pressure Science and Technology, Madrid* [accepted for publication].

Ague J. J. and Nicolescu S. (2014) Carbon dioxide released from subduction zones by fluid-mediated reactions. *Nat. Geosci.* **7**, 355-360.

Andersen, T. and Neumann, E.-R. (2001) Fluid inclusions in mantle xenoliths. *Lithos* **55**, 301–320.

Aranovich L. Y. and Newton R. C. (1999) Experimental determination of CO_2-H_2O activity-composition relations at 600–1000 °C and 6–14 kbar by reversed decarbonation and dehydration reactions. *Am. Mineral.* **84**, 1319-1332.

Audet P., Bostock M. G., Boyarko D. C., Brudzinski M. R. and Allen R. M. (2010) Slab morphology in the Cascadia fore arc and its relation to episodic tremor and slip. *J. Geophys. Res.*, **115**, B00A16.

Barkan E. and Luz B. (2012) High-precision measurements of $^{17}O/^{16}O$ and $^{18}O/^{16}O$ ratios in CO_2. *Rapid Commun. Mass Spectrom.* **26**, 2733-2738.

Beck W. C., Grossman E. L. and Morse J. W. (2005) Experimental studies of oxygen isotope fractionation in the carbonic acid system at 15°, 25°, and 40°C. *Geochim. Cosmochim. Acta* **69**,

750   3493-3503.

751   Benezeth P., Stefansson A., Gautier Q. and Schott J. (2013) Mineral solubility and aqueous speciation
752   under hydrothermal conditions to 300°C-The carbonate system as an example. *Rev. Mineral.*
753   *Geochem.* **76**, 81-133.

754   Bodnar R. J., Burnham C. W. and Sterner S. M. (1985) Synthetic fluid inclusions in natural quartz.
755   III. Determination of phase equilibrium properties in the system H_2O-NaCl to 1000°C and 1500
756   bars. *Geochim. Cosmochim. Acta* **49**, 1861-1873.

757   Bollengier O., Choukroun M., Grasset O., Le Menn E., Bellino G., Morizet Y., Bezacier L. Oancea
758   A. Taffin C. and Tobie G. (2013) Phase equilibria in the H_2O–CO_2 system between 250–330 K
759   and 0–1.7 GPa: Stability of the CO_2 hydrates and H_2O-ice VI at CO_2 saturation. *Geochim.*
760   *Cosmochim. Acta* **119**, 322-339.

761   Brodholt J. and Wood B. (1993) Molecular dynamics simulations of the properties of CO_2-H_2O
762   mixtures at high pressures and temperatures. *Am. Mineral.* **78**, 558-564.

763   Capobianco R., Gruszkiewicz M. S., Wesolowski D. J., Cole D. R., and Bodnar R. J. (2013)
764   Volumetric properties and fluid phase equilibria of CO_2 + H_2O. Thirty-Eighth Workshop on
765   Geothermal Reservoir Engineering, Stanford University, Stanford

766   Clayton R. N., Goldsmith J. R., Karel K. J., Mayeda T. K. and Newton R. C. (1975) Limits on the
767   effect of pressure on isotopic fractionation. *Geochim. Cosmochim. Acta* **39**, 1197-1201.

768   Corey, A.T. (2003) *Mechanics of immiscible fluids in porous media*, Water Resources Publications,
769   Highland Ranch, Colorado.

770   Costantino M. and Rice S. F. (1991) Supercritical phase separation in H_2O-N_2 mixtures. *J. Phys.*
771   *Chem.* **95**, 9034-9036.

772   Craig H. (1957) Isotopic standards for carbon and oxygen and correction factors for mass-
773   spectrometric analysis of carbon dioxide. *Geochim. Cosmochim. Acta* **12**, 133-149.

774   Christoforakos M. and Franck E. U. (1986) An equation of state for binary fluid mixtures to high
775   temperatures and high pressures. *Ber. Bunsenges. Phys. Chem.* **90**, 780-789.

776   Datchi F., Loubeyre P. and LeToullec R. (2000) Extended and accurate determination of the melting
777   curves of argon, helium, ice (H_2O), and hydrogen (H_2). *Phys. Rev. B* **61**, 6535-6546.

778   Dos Ramos M. C., Blas F. J. and Galindo A. (2007) Phase Equilibria, Excess Properties, and Henry's
779   Constants of the Water + Carbon Dioxide Binary Mixture. *J. Phys. Chem.* **111**, 15924-15934.

780   Duan Z. and Zhang Z. (2006) Equation of state of the H_2O, CO_2, and H_2O–CO_2 systems up to 10 GPa
781   and 2573.15 K: Molecular dynamics simulations with ab initio potential surface. *Geochim.*
782   *Cosmochim. Acta* **70**, 2311–2324.

783   Eggler D. H., Kushiro I. and Holloway J. R. (1979) Free energies of decarbonation reactions at
784   mantle pressures: I. Stability of the assemblage forsterite-enstatite-mangesite in the system MgO-
785   SiO_2-CO_2-H_2O to 60 kbar. *Am. Mineral.* **64**, 288-293.

786   Facq S., Daniel I., Montagnac G., Cardon H. and Sverjensky D. A. (2014) In situ Raman study and
787   thermodynamic model of aqueous carbonate speciation in equilibrium with aragonite under
788   subduction zone conditions. *Geochim. Cosmochim. Acta* **132**, 375-390.

789   Frost B. R. and Frost C. D. (2014) *Essentials of Igneous and Metamorphic Petrology*, Cambridge
790   University Press, Cambridge.

791   Frost D. J. and Wood B. J. (1997) Experimental measurements of the properties of H_2O-CO_2 mixtures
792   at high pressures and temperatures. *Geochim. Cosmochim. Acta* **61**, 3301-3309.

793   Galvez M. E., Manning C. E., Connolly J. A. D. and Rumble D. (2015) The solubility of rocks in
794   metamorphic fluids: A model for rock-dominated conditions to upper mantle pressure and
795   temperature. *Earth Planet. Sci. Lett.* **430**, 486-498.

796 Gehrig M., Lentz H. and Franck E. U. (1986) The system water-carbon dioxide-sodium chloride to
797   773K and 300 MPa. *Ber. Busenges. Phys. Chem.* **90**, 525-533.
798 Giordano V. M., Datchi F. and Dewaele A. (2006) Melting curve and fluid equation of state of carbon
799   dioxide at high pressure and high temperature. *J. Chem. Phys.* **125**, 054504-1-8.
800 Harte B. (2010) Diamond formation in the deep mantle: the record of mineral inclusions and their
801   distribution in relation to mantle dehydration zones. *Mineral. Mag.* **74**, 189-215.
802 Hirschmann M. M. and Dasgupta R. (2009) The H/C ratios of Earth's near-surface and deep
803   reservoirs, and consequences for deep Earth volatile cycles. *Chem. Geol.* **262**, 4-16.
804 Holland T. and Powell R. (2003) Activity–composition relations for phases in petrological
805   calculations: an asymmetric multicomponent formulation. *Contrib. Mineral Petrol.* **145**, 492-501.
806 Jacobs G. K. and Kerrick D. M. (1981) APL and FORTRAN programs for a new equation of state for
807   H_2O, CO_2, and their mixtures at supercritical conditions. *Comput. Geosci.* **7**, 131-143.
808 Kelemen P. B and Manning C. E. (2015) Reevaluating carbon fluxes in subduction zones, what goes
809   down, mostly comes up. *Proc. Natl. Acad. Sci. U.S.A.* **112**, E3997-E4006.
810 Kerrick D. M. and Jacobs G. K. (1981) A modified Redlich-Kwong Equation for H_2O-CO_2 mixtures
811   at elevated pressures and temperatures. *Amer. J. Sci.* **281**, 735-767.
812 Looyenga H. (1965) Dielectric constants of heterogeneous mixtures. *Physica* **31**, 401-406.
813 Mader U. K. (1991) H_2O-CO_2 mixtures: a review of P-V-T-X data and an assessment from a phase-
814   equilibrium point of view. *Can. Mineral.* **29**, 767-790.
815 Manning, C. E. and Shock E. L. (2013) The chemistry of carbon in aqueous fluids at crustal and
816   upper-mantle conditions: Experimental and theoretical constraints. *Rev. Mineral. Geochem.*, **75**,
817   109-148.
818 Mather A. E. and Franck E. U. (1992) Phase equilibria in the system carbon dioxide-water at elevated
819   pressures. *J. Phys. Chem.* **96**, 6-8.
820 McCord T. B., Hayne P., Combe J.-P., Hansen G. B., Barnes J. W., Rodriguez S., Le Mouélic S.,
821   Baines K. H., Buratti B. J., Sotin C., Nicholson P., Jaumann R., Nelson R. and the Cassini VIMS
822   Team (2008). Titan's surface: Search for spectral diversity and composition using the Cassini
823   VIMS investigation. *Icarus*, **194**, 212-242.
824 McLaren E. H. and Murdock E. G. (1960) The Freezing Points of High Purity Metals as Precision
825   Temperature Standards. *Can. J. Phys.* **38**, 577-587.
826 Mountain R. D. and Harvey A. H. (2015) Molecular dynamics evaluation of dielectric constant
827   mixing rules of H_2O-CO_2 at geologic conditions. *J. Solution Chem.* **44**, 2179-2193.
828 Poulton D. J. and Baldwin H. W. (1967) Oxygen exchange between carbonate and bicarbonate ions
829   and water. I. Exchange in the absence of added catalysts. *Can. J. Chem.* **45**, 1045-1050.
830 Porco C., Helfenstein P., Thomas P. C., Ingersoll A. P., Wisdom J., West R., Neukum G., Denk T.,
831   Wagner R., Roatsch T., Kieffer S., Turtle E., McEwen A., Johnson T. V, Rathbun J., Veverka J.,
832   Wilson D., Perry J., Spitale J., Brahic A., Burns J. A., DelGenio A. D., Dones L., Murray C. D.,
833   and Squyres S. (2006). Cassini observes the active south pole of Enceladus. *Science*, **311**, 1393-
834   1401, doi: 10.1126/science1123013.
835 Rosenbaum J. M. (1993) Room temperature oxygen isotope exchange between liquid CO_2 and H_2O.
836   *Geochim. Cosmochim. Acta,* **57**, 3195-3198.
837 Schmidt C. and Bodnar R. J. (2000) Synthetic fluid inclusions: XVI. PVTX properties in the system
838   H_2O-NaCl-CO_2 at elevated temperatures, pressures, and salinities. *Geochim. Cosmochim. Acta,*
839   **64**, 3853–3869.
840 Sohl F., Choukroun M., Kargel J., Kimura J, Pappalardo R., Vance S. and Zolotov M. (2010)
841   Subsurface Water Oceans on Icy Satellites: Chemical Composition and Exchange Processes.

842   *Space Sci. Rev.* **153**, 485-510.

843   Sterner S. M. and Bodnar R. J. (1991) Synthetic fluid inclusions. X: Experimental determination of P-
844   V-T-X properties in the CO_2-H_2O system to 6 kb and 700°C. *Amer. J. Sci.* **291**, 1-54.

845   Sverjensky D. A., Stagno V. and Huang F. (2014) Important role for organic carbon in subduction-
846   zone fluids in the deep carbon cycle. *Nat. Geosci.* 7, 909-913.

847   Syracuse, E. M., Van Keken, P. E., and Abers, G. A. (2010) The global range of subduction zone
848   thermal models. *Phys. Earth Planet. Inter.* **183**, 73–90.

849   Takenouchi S. and Kennedy G. C. (1964) The binary system CO_2-H_2O at high temperatures and
850   pressures. *Amer. J. Sci.* **262**, 1055-1074.

851   Todheide K. and Franck E. U. (1963) Das Zweiphasengebiet und die kritische kurve in system
852   kohlendioxide-wasser bis zu drucken von 3500 bar. *Z. Phys. Chem.* (Neue Folge) **37**, 387-401.

853   Truesdell A. H. (1974) Oxygen isotope activities and concentrations in aqueous salt solutions at
854   elevated temperatures: consequences for isotope geochemistry. *Earth Planet. Sci. Lett.* **23**, 387-
855   396.

856   Vance S., Bouffard M., Choukroun, M. and Sotin C. (2014) Ganymede's internal structure including
857   thermodynamics of magnesium sulfate oceans in contact with ice. *Planet. Space Sci.* **96**, 62-70.

858   van Hinsberg M. G. E., Verbrugge R. and Schouten J. A. (1993) High temperature-high pressure
859   experiments on H_2O-N_2. *Fluid Phase Equilib.* **88**, 115-121.

860   van Konynenburg P. H. and Scott R. L. (1980) Critical lines and phase equilibria in binary van der
861   Waals mixtures. *Philos. Trans. R. Soc.*, A **298**, 495-540.

862   Wagner W., Saul A., and Pruss A. (1994) International equations for the pressure along the melting
863   and along the sublimation curve of ordinary water substance. *J. Phys. Chem. Ref. Data* **23**, 515-
864   527.

865   Wang H., Zeuschner J., Eremets M., Troyan I. and Willams J. (2016) Stable solid and aqueous
866   H_2CO_3 from CO_2 and H_2O at high pressure and high temperature. Sci. Rep. **6**, 19902-1-8.

867   Wendland M., Hasse H. and Maurer G. (1999) Experimental pressure-temperature data on three- and
868   four-phase equilibria of fluid, hydrate, and ice phases in the system carbon dioxide-water. *J.
869   Chem. Eng. Data* **44**, 901-906.

870   Whitson C. H. and Brule M. R. (2000) *Phase Behavior*. SPE Monograph Series **20**, Society of
871   Petroleum Engineers, Richardson, TX.

872   Zhang C. and Duan Z. (2009) A model for C–O–H fluid in the Earth's mantle. *Geochim. Cosmochim.
873   Acta,* **73**, 2089-2102.

874   Zhang C. and Duan Z. (2010) GFluid: An Excel spreadsheet for investigating C–O–H fluid
875   composition under high temperatures and pressures. *Comput. Geosci.* **36**, 569-572.

Table 1
X_{CO_2} as determined by ^{13}C and by ^{18}O (values suggested by the fitted surface are given parenthetically for three outliers).

run #	X_{CO_2} (%) by ^{13}C	X_{CO_2} (%) by ^{18}O	data type
1	41	45	1†
2	75	89	2
3	25	43 (37)	3*
4	28	51 (28)	3
5	62	89	2*
6	41	49	2†
7	64	68	1†
8	17	19	1*
9	54	63	2†
10	67	69 (77)	3*
11	63	69	2†
12	48	49	1*
13	90	92	1*
14	44	43	1*
15	22	22	1*
16	31	30	1*
17	61	57	1†
18	88	90	1*
19	78	91	2
20	21	22	1*
21	35	35	1
22	33	35	1*
23	56	53	1†
24	61	60	1*
25	30	29	1
26	25	25	1

* plotted in Fig. 6a; † plotted in Fig. 6b.